

A Janus Separator for Inhibiting Shuttle Effect and Lithium Dendrite in Lithium–Sulfur Batteries

Ru Xiao^{+, [a, b]} Shan Yang^{+, [a, c]} Tong Yu^{+[a]} Tianzhao Hu,^[a, d] Xiaoyin Zhang,^[a, b] Ruogu Xu,^[a, b] Yaozu Wang,^[a, b] Xiaodong Guo,^[c] Zhenhua Sun,^{*[a, b]} and Feng Li^{*[a, b]}



Lithium–sulfur (Li–S) batteries are promising candidates for next-generation energy storage systems. However, unsurpassed challenges including the shuttle effect and Li dendrite growth are still faced for marketization. Herein, La₂Zr₂O_{7-x} (OV-LZO) nanotubes with surface oxygen vacancies were fabricated to serve as Janus separator coatings for Li–S batteries. The overlapping OV-LZO nanotubes construct an efficient lithium polysulfides adsorption and catalysis network at the interface of the cathode/separator and a Li⁺ transport network by increasing the Li⁺ transfer number and boosting Li⁺ diffusion at the interface of the anode/separator to tackle the shuttle effect and

lithium dendrite issues. The excellent thermal stability of OV-LZO lowers the possibility of a short circuit. As a result, the elaborate Janus OV-LZO coating enabled Li–S batteries with an areal capacity of 8.33 mAh cm⁻² after 50 cycles at 0.2 C under conditions of high sulfur loading (9.1 mg cm⁻²), lean electrolyte (E/S of 4.5 mL g⁻¹) and low N/P ratio of 2. Moreover, the gravimetric energy density of the battery was greatly increased compared to that of the commercial separator with little increase in the mass loading of separator. This strategy can be integrated with the optimization of other battery components to light the way for the construction of practical Li–S batteries.

Introduction

Lithium–sulfur (Li–S) batteries have been regarded as promising candidates for next generation energy storage systems due to their high theoretical capacity (Li: 3860 mAh g⁻¹ and S: 1675 mAh g⁻¹) and energy density (2600 Wh kg⁻¹).^[1–3] However, unsurpassed challenges are still faced for marketization, with shuttle effects caused by soluble lithium polysulfide (Li₂S_x, 4 ≤ x ≤ 8; LiPS) intermediates and Li dendrite growth as the two major problems that deteriorate the cycling stability and thermal safety of batteries.^[4–8]

Designing functional separator coating layer has been proved to be an effective method to inhibit LiPS shuttling.^[9–11]

[a] R. Xiao,⁺ S. Yang,⁺ Dr. T. Yu,⁺ T. Hu, X. Zhang, R. Xu, Y. Wang,

Prof. Dr. Z. Sun, Prof. F. Li

Shenyang National Laboratory for Materials Science

Institute of Metal Research

Chinese Academy of Sciences

Shenyang 110016, China

E-mail: zhsun@imr.ac.cn

fli@imr.ac.cn

[b] R. Xiao,⁺ X. Zhang, R. Xu, Y. Wang, Prof. Dr. Z. Sun, Prof. F. Li

School of Materials Science and Engineering

University of Science and Technology of China, China

[c] S. Yang,⁺ Prof. X. Guo

School of Chemical Engineering

Sichuan University

Chengdu 610065, China

[d] T. Hu

School of Materials Science and Engineering

Zhengzhou University

Zhengzhou 450001, China

[+] These authors contributed equally to this work.

Supporting information for this article is available on the WWW under <https://doi.org/10.1002/batt.202100389>

An invited contribution to a Special Collection dedicated to Lithium–Sulfur Batteries

Carbon materials with high conductivity, such as carbon nanotubes,^[12] carbon fibers,^[13] and graphene,^[14] as the coating material can physically block LiPS within the cathode region, and serve as the upper current collector to make LiPS participate in the subsequent redox reaction. However, the weak van der Waals force between carbon and LiPS results in a passive barrier and limited capture of LiPS.^[15,16] A more aggressive strategy is to modify the separator with polar electrocatalysts (metal oxides,^[17,18] sulfides,^[19] nitrides,^[15] phosphides,^[20] MXene,^[21] etc.) that can chemically adsorb LiPS and catalyze the sulfur reduction reaction. In this way, the sluggish kinetics of the sulfur redox reaction that results in LiPS detaining and shuttling in the electrolyte can be effectively tackled, and simultaneously improve the rate capability of Li–S batteries.^[22–25] The coating layer with physical confinement, chemical adsorption and electrocatalysis toward LiPSs has shown a synergistic effect but may also slow Li⁺ conduction in a dense blocking matrix.^[26–28] Therefore, it is also highly desirable to concurrently expedite LiPSs conversion together with Li ion (Li⁺) transport at the coating/electrolyte interface through rational material and structural design.

Potential safety problems caused by Li dendrite growth limit the practical application of Li–metal anode.^[29] Moreover, the Li anode corroded by LiPS causes structural non-uniform SEI and aggravates dendrite growth, which makes the SEI film repeatedly form and destroy, further deteriorating the Li plating/stripping environment.^[30,31] As an important component of the cell, the separator served as a “shield” to prevent short-circuiting by massive and sharp Li dendrite “spear”. A commercial polyolefin separator with poor mechanical properties and a low melting point may suffer from lithium dendrite puncture and inferior thermal stability, which could bring about safety risks at elevated temperature. Therefore, the design and

optimization of protective separator coatings has been regarded as a promising way to extend the cycling life of Li anodes by redistributing the Li^+ flux/electric field,^[32] increasing transference number of Li^+ ,^[33] and serving as lithophilic sites^[34] to guide uniform Li stripping/plating, and enhancing the thermal and mechanical stability of separators.^[35] Compared with other strategies such as engineering ingenious Li hosts,^[36] electrolyte additives,^[37] and designing stable artificial SEI,^[38] targeted separator modification can be extended to a variety of battery systems and adapted to the production process.

In consideration of commercialization, it would be appealing to rationally select and design a multi-functional material to meet distinct demands of the cathode and anode. Polar metal oxides with simple synthesis have both a high LiPS adsorption energy and lithophilic nature,^[39] showing great potential as Janus coating layers of commercial polyolefin separators to weaken the shuttle effect and homogenize Li deposition. In addition, the tolerance of the modified separator toward Li dendrites is extremely enhanced by the high mechanical strength of oxides. Oxide ceramic particles with low thermal conductivity could also enhance the thermal stability of separators.^[40] However, further improvement in the catalytic activity on polysulfide conversion and Li^+ conduction capability of metal oxides is essential to efficiently regulate the interfacial sulfur redox reactions and Li stripping/plating. Therefore, selecting a suitable metal oxide followed by crystal structure modification and morphology regulation as the Janus separator coating layer to solve the above issues is of great significance for designing functional separators for Li–S batteries.

Herein, pyrochlore-type $\text{La}_2\text{Zr}_2\text{O}_{7-x}$ (OV-LZO) nanotubes with surface oxygen vacancies were fabricated by electrospinning and the Ar/H₂ etching method to serve as Janus separator coatings for Li–S batteries. The overlapping OV-LZO nanotubes construct an efficient LiPS adsorption/catalysis network at the interface of the cathode/separator and a redistributed Li^+ transport network at the interface of the anode/separator. Oxygen vacancies endow OV-LZO with higher LiPS adsorptivity and catalytic activity toward the redox reaction of sulfur species than $\text{La}_2\text{Zr}_2\text{O}_7$ (LZO). Moreover, oxygen vacancies can restrict the free migration of Li–salt anions to accelerate Li^+ transport and achieve highly stable Li plating/stripping. The excellent thermal stability of OV-LZO lowers the possibility of shortage under abnormal conditions, which ensures the long-term cycling. As a result, the elaborate Janus separator coating enabled Li–S batteries with initial areal capacities of 8.7 mAh cm⁻², and 8.33 mAh cm⁻² after 50 cycles at 0.2 C under high sulfur loading (9.1 mg cm⁻²), lean-electrolyte (E/S of 4.5 mL g⁻¹) and a low N/P ratio of 2. Under such strict conditions, the gravimetric energy density of the battery was greatly increased compared to that of the PP separator with little increase in the areal mass loading of the separator by OV-LZO. This strategy can be integrated with the optimization of other battery components to light the way for construction of the practical Li–S batteries.

Results and Discussion

Figure 1(a) schematically illustrates the fabrication process of multi-functional $\text{La}_2\text{Zr}_2\text{O}_{7-x}$ with surface oxygen vacancies (OV-LZO). The precursor fiber of $\text{La}_2\text{Zr}_2\text{O}_7$ (LZO) was synthesized by electrospinning the corresponding metal nitrates and polyvinylpyrrolidone (PVP) solution (Figure S1), and LZO nanotubes were prepared by annealing the precursor fiber at 900 °C in air atmosphere. To obtain OV-LZO, LZO was further reduced at 700 °C in an Ar/H₂ atmosphere to remove the surface lattice oxygen. Transmission electron microscopy (TEM) image shows that OV-LZO nanotubes with rough surfaces and diameters of approximately 200 nm are assembled by nanoparticles, which are conducive to the exposure of catalytic active sites, infiltration of electrolytes and construction of fast ion transport channels (Figure 1b). A high-resolution transmission electron microscopy (HRTEM) image of OV-LZO distinctly shows a well-resolved lattice fringes spacing of 0.310 nm corresponding to (222) plane of LZO (Figure 1c). Furthermore, the same crystalline phase of OV-LZO and LZO was certified by X-ray diffraction (XRD) patterns (Figure S2). The SEM image of OV-LZO nanotube presents an overlapping network structure, and the homogeneous distribution of La, Zr, and O elements throughout OV-LZO was revealed by energy-dispersive X-ray spectroscopy (EDS) elemental mapping (Figure 1d). The nitrogen adsorption/desorption isotherm and the corresponding pore size distribution show that OV-LZO has a specific surface area of 30.2 m² g⁻¹ and a uniform pore size distribution dominated by mesopores and macropores, which promises multiple adsorption sites and favorable ion transfer (Figure S3).

The oxygen vacancies in OV-LZO were detected by electron paramagnetic resonance (EPR) analysis, which is an effective method for detecting the unpaired electrons and was widely used to investigate oxygen vacancies.^[41,42] As shown in Figure 1(e), the OV-LZO curve shows an oxygen vacancy signal at the *g* value of 2.004, whereas LZO shows almost no sign of oxygen deficiency. X-ray photoelectron spectroscopy (XPS) and Raman spectra were further performed to investigate the changes in surrounding chemical environment of oxygen vacancies. The generation of oxygen vacancies would increase the electron cloud density of the metal atom adjacent to the oxygen vacancy, and the energy level for valence electron of metal atoms decrease accordingly, resulting in lower binding energy for XPS spectra. The high-resolution XPS spectrum of La 3d splits into the 3d_{5/2} and 3d_{3/2} states with a spin-orbit splitting of 16.9 eV (Figure 1f). Final state I is the core hole state (3d¹4f⁰) ascribed to the La–O bond, while final state II is the core hole state (3d¹f¹) with electron transfer from the O 2p valence band to an empty 4f orbital, which is ascribed to the hydroxylated surface by the La–OH band.^[43] These two peaks in OV-LZO shift to lower binding energy relative to LZO, indicating that the O coordinated with La is missing and forms a vacancy. In contrast, an invisible peak offset is displayed in the high-resolution Zr 3d XPS spectra, indicating a maintained chemical environment (Figure S4). Meanwhile, in the high-resolution O 1s XPS spectra, two peaks at 529.3 (O_I) and 531.4 eV (O_{II}) are attributed to contributions from lattice oxygen and defective oxygen,

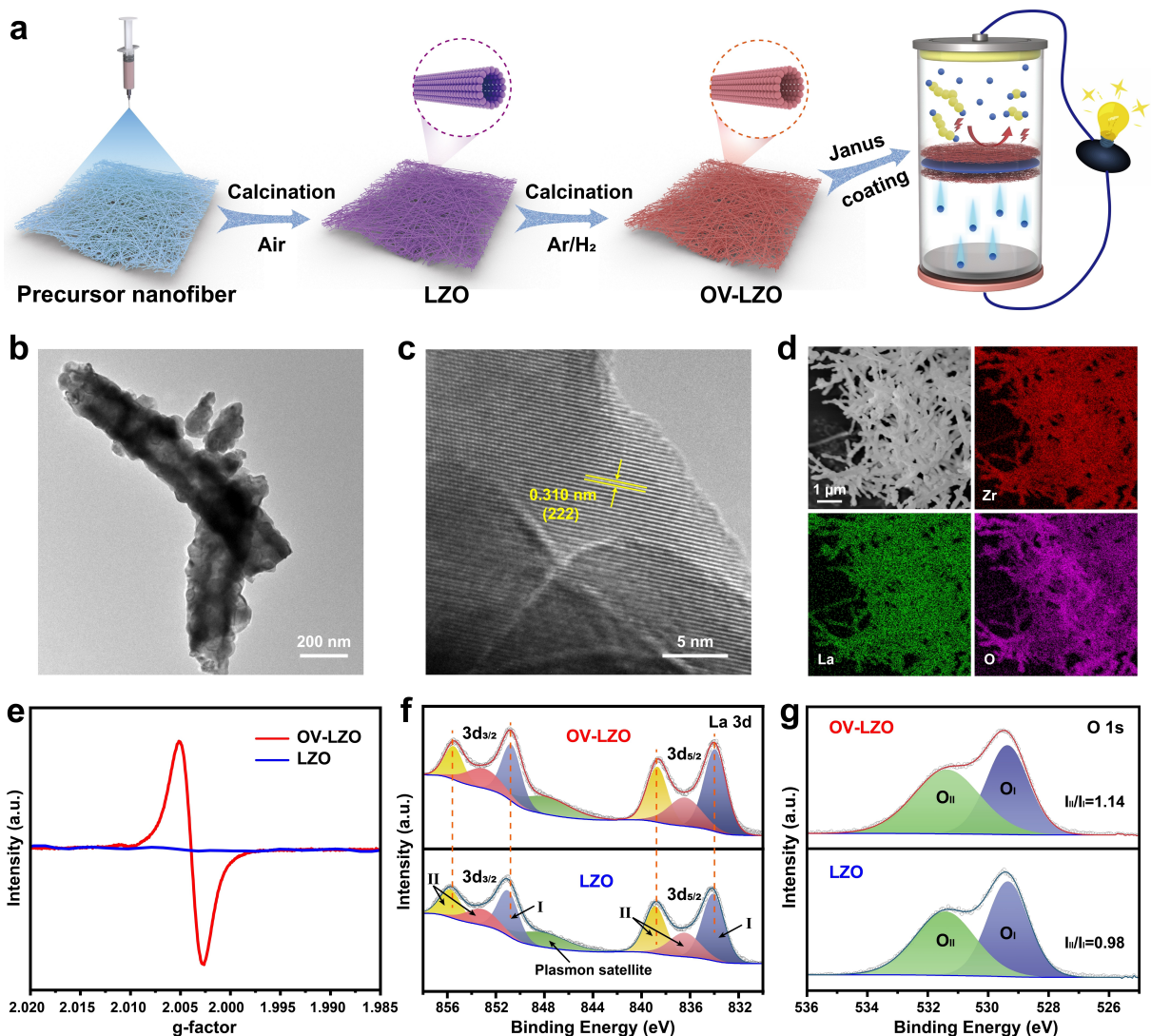


Figure 1. a) Schematic illustration of the synthetic procedures of OV-LZO as Janus interlayer for Li–S batteries. b) TEM and c) HRTEM images of OV-LZO. d) SEM image and elemental mapping of OV-LZO nanotubes. e) EPR spectra of LZO and OV-LZO. High resolution of f) La 3d and g) O 1s XPS spectra of OV-LZO nanotubes.

respectively (Figure 1g).^[44] The peak intensity ratio of O_{II}/O_I is increased from 0.98 for LZO to 1.14 for OV-LZO, implying the increased formation of oxygen vacancies in OV-LZO. The Raman spectra sensitively detect changes in chemical bonds as well. Five Raman modes (M1–M5) of the pyrochlore phase can be identified in LZO and OV-LZO (Figure S5).^[45] The Raman peak at $\sim 300 \text{ cm}^{-1}$ is made up of two Raman modes: one intense E_g mode assigned to O–Zr–O bending in [ZrO₆] octahedrons (M1) and a weak F_{2g} mode associated with La–O' stretching (M2). The band at $\sim 380 \text{ cm}^{-1}$ is an F_{2g} mode ascribed to the vibrations of oxygen anions (O–O') (M3). M4 at $\sim 500 \text{ cm}^{-1}$ is another F_{2g} mode ascribed to Zr–O stretching. M5 at $\sim 515 \text{ cm}^{-1}$ corresponds to La–O stretching. Compared with LZO, the Raman peaks of OV-LZO are evidently weakened, and the broadening of M5 peak further reveal the reduced La–O bonds.

The ability to anchor LiPS is the critical indicator for inhibiting the shuttle effect and the premise of efficient

electrocatalysis for Li–S batteries. By adjusting the local electrons state, the oxygen vacancy would make the La site rich in local electrons, which can induce the capture of polysulfides by strong dipole-dipole interaction. The optimized stable adsorption configurations of Li₂S₄ adsorbed on LZO and OV-LZO were calculated based on density functional theory (DFT) (Figures 2a and S6). The most exposed (222) crystal plane with the least surface energy and most stable structure was selected as the adsorption surface. OV-LZO allows more chemical bonding interactions between La and S, resulting in higher adsorption energy of -2.333 eV than LZO (-1.348 eV), suggesting a high-efficiency LiPS immobilization effect by coordinating unsaturated atoms. The charge density difference clearly shows the charge transfer between the S atom and the La atom adjacent to the oxygen vacancy, further verifies the local charge induced La–S interaction (Figure S7). Visual adsorption tests were conducted to verify the superior surface affinity of OV-LZO toward LiPS (Figure S8). Apparently, the color

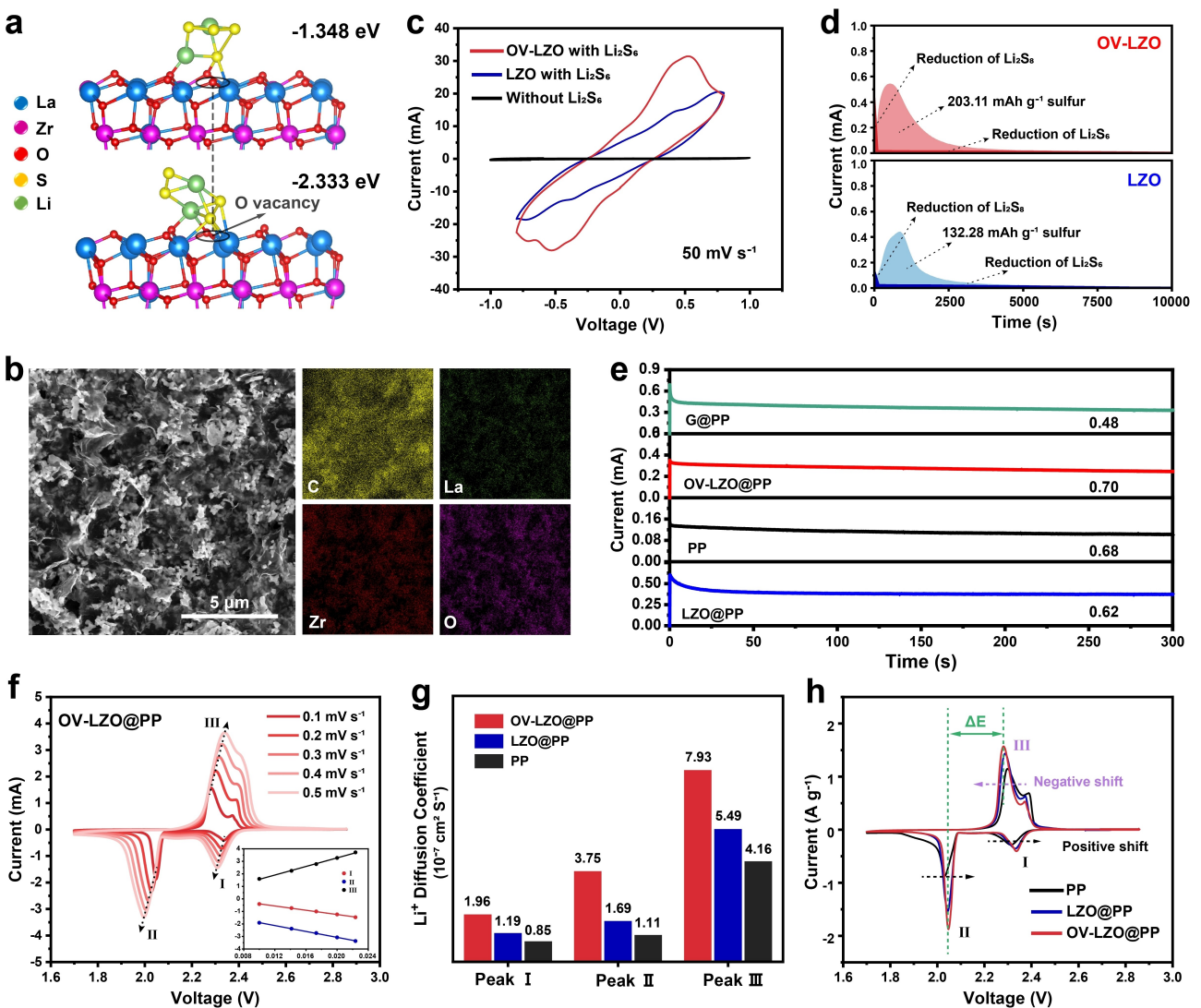


Figure 2. a) The optimized stable adsorption configurations of Li_2S_4 adsorbed on the (222) surface of LZO and OV-LZO. b) SEM image and element distribution of the OV-LZO@PP separator. c) CV curves of Li_2S_6 symmetry cells with LZO and OV-LZO electrodes at scan rate of 50 mV s^{-1} . d) Potentiostatic Li_2S nucleation curves of the LZO and OV-LZO electrodes. e) t_{Li^+} for PP, G@PP, LZO@PP and OV-LZO@PP. f) CV curves of OV-LZO@PP at various scan rates within a potential window of 1.7–2.8 V and g) D_{Li^+} value of Li_2S_6 at different current peaks. h) CV curves of Li-S cells with OV-LZO@PP, LZO@PP and PP at 0.1 mV s^{-1} .

of the Li_2S_6 solution with OV-LZO became colorless and transparent after 30 min in contrast with LZO and graphene. The adsorption solution with OV-LZO displays the lowest UV intensity among these samples, demonstrating the strongest LiPS anchoring ability. XPS analysis of OV-LZO after soaking in Li_2S_6 solution was carried out (Figure S9). The peaks corresponding to La–O and La–OH bonds in the La 3d_{5/2} spectra shift to lower binding energy indicating the reduction of electron cloud density of La in OV-LZO, induced by formation of strong La–S bonding. In contrast, the Zr 3d spectra show an implicit peak shift after adsorbing Li_2S_6 , indicating that Zr atoms in OV-LZO hardly participate in bonding with polysulfide, consistent with the DFT results.

LZO and OV-LZO were mixed with graphene with a mass ratio of 8:1 as the coating layer of a commercial PP separator (denoted as LZO@PP and OV-LZO@PP, respectively). Scanning electron microscopy (SEM) images and corresponding energy-

dispersive X-ray spectroscopy (EDS) elemental mapping show that overlapping OV-LZO nanotubes as adsorption/catalytic sites were uniformly loaded on graphene sheets to ensure fast electron/ion transport (Figures 2b and S10). An H-type glass device was introduced to clamp the separator in the middle to carry out the permeation test of Li_2S_6 solution (Figure S11). The fast color change for the PP separator indicates the difficulty of confining the shuttle effect. Notably, the lighter yellow color on the right side of the H-type glass device with the OV-LZO@PP than LZO@PP separator after 24 h. This result demonstrates that the shuttling of polysulfide has been efficiently suppressed by stronger chemical adsorption of OV-LZO and physical blocking of the graphene sheets.

In addition to the polysulfide absorptivity, the electrocatalytic activity of OV-LZO was evaluated. For liquid-liquid polysulfide conversion probed by $\text{Li}_2\text{S}_6 \parallel \text{Li}_2\text{S}_6$ symmetric cells with OV-LZO (or LZO) as both working and counter electrodes,

OV-LZO renders 53% and 97% enhancement compared to LZO in maximum response current and total transferred charge, respectively (Figure 2c). For liquid-solid Li₂S deposition investigated by chronoamperometry of Li || Li₂S₈ cells with OV-LZO (or LZO) dispersed on carbon paper as the working electrode, OV-LZO possesses an earlier and higher potentiostatic peak (0.55 mA at 532 s) than LZO (0.44 mA at 847 s), demonstrating a faster Li₂S nucleation/growth rate (Figure 2d). The enhanced polysulfide conversion kinetics obtained by improving the catalytic activity of the coating material are conducive to reducing the retention and diffusion of LiPS in the electrolyte, and inhibiting the shuttle effect more aggressively.

Li⁺ transference across the separator is an important factor to affecting the kinetic performance but is often hindered by dense modified coatings. It has been reported that oxygen vacancies of oxide ceramics can strongly interact with Li–salt anions and contribute to more facile Li⁺ transport.^[45] To acquire the detailed Li⁺ transference numbers (t_{Li^+}), PP, graphene coated on PP (G@PP), LZO@PP, and OV-LZO@PP separators were sandwiched between two Li electrodes, and a constant potential of 10 mV was applied. The t_{Li^+} represents the ratio of the total charge carried by Li⁺ to that carried by both Li⁺ and the anions in the electrolyte, thus reflecting the Li⁺ transport properties of various separators. G@PP has the lowest t_{Li^+} (0.48), suggesting that dense graphene sheets produce a strong barrier for Li⁺ transport and conductivity. The t_{Li^+} of the LZO@PP separators (0.62) is comparable to that of the pure PP separator (0.68), indicating the effectively prevented stacking of graphene layers and the fast Li⁺ surface diffusion provided by the LZO nanotube network. The oxygen vacancies in OV-LZO may lead to abundant surface unsaturated coordinative metal sites, which are capable of fixing Li–salt anions (TFSI⁻) in the electrolyte according to the Lewis acid-base interaction.^[46] The TFSI⁻ anions tend to bind to the surface of OV-LZO, reduce the Li⁺–TFSI⁻ interaction and release more available Li⁺, thus increasing the Li⁺ transference number (t_{Li^+}) in the electrolyte. Therefore, the OV-LZO@PP separator possesses the largest t_{Li^+} of 0.70 even higher than that of the PP separator (Figure 2e). In addition, the OV-LZO@PP separator exhibits sufficient contact with the electrolyte to achieve a more efficient electrochemical process (Figure S12).

The Li⁺ diffusion coefficients (D_{Li^+}) for PP, LZO@PP, and OV-LZO@PP separators were quantitatively calculated by investigating the CV curves of Li–S half cells at various scan rates (Figures 2f and S13). The two cathodic peaks in the CV curves correspond to the reduction of S₈ to soluble LiPS (peak I) and the formation of solid lithium sulfides Li₂S₂/Li₂S (peak II), while the anodic peaks represent the reverse conversion of Li₂S₂/Li₂S to S₈ (peak III). According to the Randles–Sevcik equation:

$$I_p = (2.69 \times 10^5) n^{1.5} A D_{\text{Li}^+}^{0.5} C_{\text{Li}^+} V^{0.5}$$

where I_p is the peak current, n is the number of charge transfers, A is the geometric area, D_{Li^+} is the Li⁺ diffusion coefficient, C_{Li^+} is the concentration of Li⁺ in the electrolyte, and v is the scan rate. The peak current (I_p) has a linear relation with the square root of the scan rate ($v^{0.5}$) for all separators. The

Li⁺ diffusion coefficient (D_{Li^+}) can be calculated by the slope of the fitted line, which not only reflect the Li⁺ transport property of various separators, but strongly depends on the properties of the electrolyte containing LiPS. The OV-LZO@PP separator exhibits the largest D_{Li^+} among the three separators, corresponding to the fastest Li⁺ diffusion rate, which reflects the well confined shuttle effect and reduced concentration of LiPS in the electrolyte (Figure 2g). From the CV curves, the cell with the OV-LZO@PP separator exhibits the smallest potential gap between peaks II and III, the smallest Tafel slope, and the largest peak current in comparison with the other two separators (Figures 2h and S14), which further reflects boosted reaction kinetics by the superior electrocatalytic activity of OV-LZO. The electrochemical impedance spectroscopy (EIS) measurements were performed, in which the charge transfer resistance (R_{ct}) corresponding to the semicircle at high-frequency area effectively responds to the kinetic properties (Figure S15). The lowest R_{ct} of the cell with the OV-LZO@PP separator indicates that OV-LZO can accelerate charge transfer at the electrode/separator interface and redox reaction kinetics of sulfur. The electrochemical stability of OV-LZO was proved by CV tests of OV-LZO || Li cells (Figure S16). It can be clearly observed that there is no characteristic current peak within the voltage range of 1.7–2.8 V, indicating the favorable electrochemical stability of OV-LZO during charge/discharge cycling. Furthermore, the capacity contribution of OV-LZO and a negligible capacity in sulfur-free battery illustrates that OV-LZO barely contributes to the overall capacity.

Facing the Li anode, OV-LZO coated on a PP separator without any conductive additive laps into a three-dimensional network with a uniform porous structure (Figure S17), which is conducive to the infiltration of electrolyte and redistribution of Li⁺ flux. For the nucleation process, dendrite nucleation occurs at Sand's time when the current density reaches the over-limiting current. Larger t_{Li^+} by OV-LZO may bring about delayed Sand's time, leading to a longer lifespan before Li dendrite growth.^[47–49] The diffusion barriers and diffusion pathways of Li⁺ on OV-LZO and LZO were calculated by the climbing image nudged elastic band (CI-NEB) method (Figure S18). OV-LZO has a lower diffusion barrier than LZO which contributes to a fast Li⁺ transfer network. For the growth process, the achievement of homogeneous Li⁺ flux can effectively avoid the massive growth of Li dendrites.

To verify the ability of the OV-LZO@PP separator to regulate Li deposition, galvanostatic Li nucleation tests for Li || Cu cells with different separators were employed at 1 mA cm⁻² (Figure 3a). Apparently, the voltage curve of the cell with the OV-LZO@PP separator shows the smoothest voltage dip with an overpotential of 7 mV, while it dramatically increases to 23 mV for LZO@PP and 76 mV for the PP separator, indicating that the fast Li⁺ diffusion of OV-LZO can reduce the Li nucleation barrier. The surface morphologies of deposited Li were further investigated by SEM (Figure S19). Under Li-plating at 1 mA h cm⁻², extensive mossy Li covers the whole surface of the Cu foil because of uneven Li⁺ flux through the PP separator. In contrast, the growth of Li dendrites can be greatly depressed

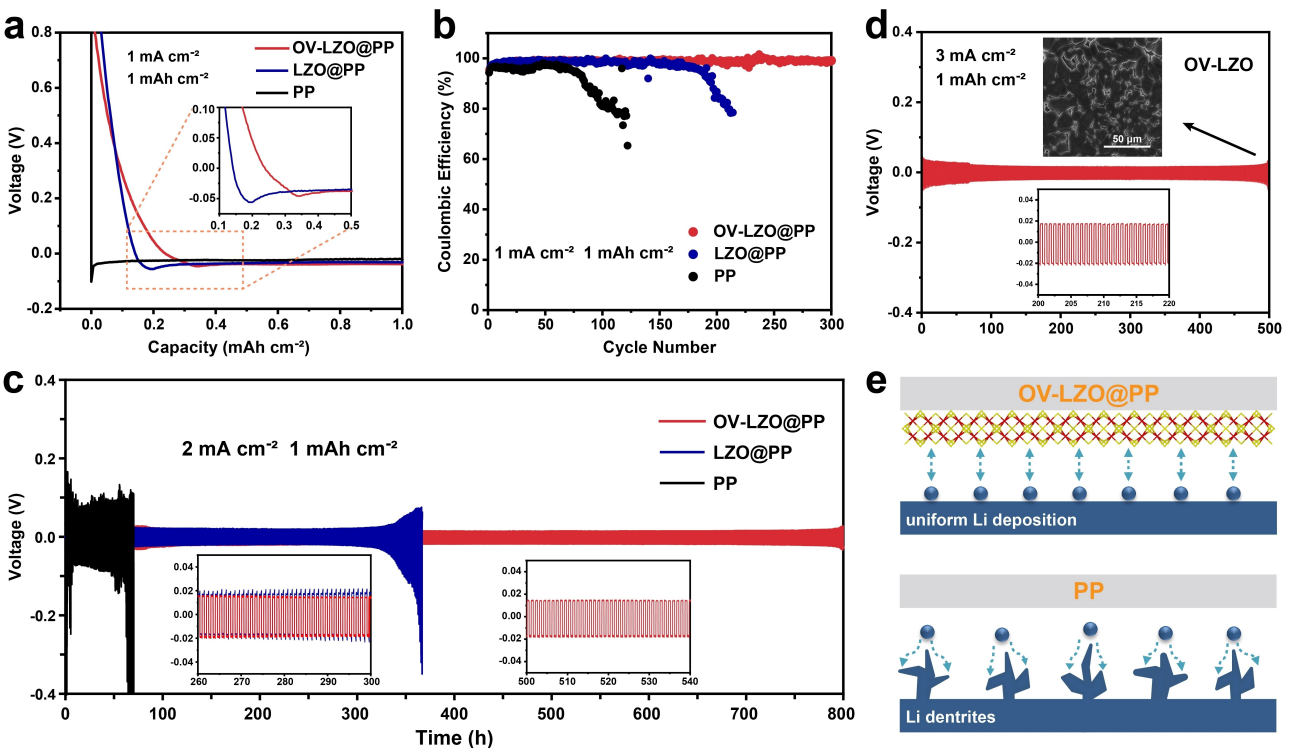


Figure 3. a) Voltage-capacity profiles of Li deposition process. b) CE at 1 mA cm^{-2} with a fixed capacity of 1 mAh cm^{-2} . c) Galvanostatic cycling of $\text{Li} \parallel \text{Li}$ cells based on OV-LZO@PP, LZO@PP and PP at 2 mA cm^{-2} under a stripping/plating capacity of 1 mAh cm^{-2} . d) Galvanostatic cycling of $\text{Li} \parallel \text{Li}$ cells with OV-LZO@PP at 3 mA cm^{-2} under a stripping/plating capacity of 1 mAh cm^{-2} . e) Functional illustrations of PP and OV-LZO@PP separators on the Li anode side.

with LZO@PP and OV-LZO@PP separators, and the latter shows smoother and denser Li deposition layer.

Coulombic efficiency (CE) is defined as the ratio of the amount of Li that can be electrochemically stripped from the anode compared with that plated on a preceding step, which serves as an accurate metric of Li anode reversibility. As displayed in Figure 3(b), the CE of the $\text{Li} \parallel \text{Cu}$ cell with the OV-LZO@PP separator exceeds 99% after 300 cycles at 1 mA cm^{-2} with a capacity of 1 mAh cm^{-2} , while the cells with LZO@PP and PP separators show early rapid attenuation, which originates from uneven Li deposition causing continuous accumulation of "dead Li" and consumption of Li by reacting with electrolyte. In contrast, the OV-LZO@PP separator can induce uniform Li deposition, thus reducing the generation of dead Li and stabilizing the SEI, to realize reversible Li plating/stripping behavior.

The long-term electrochemical stability of repetitive Li plating/stripping with different separators was studied by $\text{Li} \parallel \text{Li}$ cells and galvanostatic cycling at various current densities with fixed capacity of 1 mAh cm^{-2} . At a current density of 1 mA cm^{-2} , the PP separator exhibited initial overpotential of 66 mV, which was higher than that of the LZO@PP (37 mV) and OV-LZO@PP separators (15 mV). In addition, the polarization for the PP separator showed a sharp increase to nearly 400 mV after 102 h, which might be attributed to the excessive formation of dead Li, resulting in the fragmentation of the SEI layer accompanied by poor $\text{Li}^{+}/\text{e}^{-}$ connection. The cell with the LZO@PP separator fails after 400 h, while OV-LZO@PP presents

the smallest overpotential of 12 mV with an impressive cycling stability over 1000 h without evident voltage fluctuation (Figure S20). Under a higher current density of 2 mA cm^{-2} , a long lifespan of over 800 h for the OV-LZO@PP-based cell was attained with a small polarization of 15 mV, while the LZO@PP (22 mV for 367 h) and PP based cells (80 mV for 64 h) presented earlier observed voltage fluctuations and higher overpotentials (Figure 3c). Even at 3 mA cm^{-2} , the OV-LZO@PP-based cell still shows favorable cycling stability, and the surface of Li metal is still uniform, continuous, and flat Li deposition morphology without obvious Li dendrites (Figure 3d). All the results confirm that the OV-LZO@PP separator can facilitate uniform Li nucleation and growth due to the synergistic effect of the redistributed Li^{+} flux and the accelerated interfacial Li^{+} diffusion, subsequently achieving high cycling stability of the Li metal anode (Figure 3e). A PP separator can hardly cope with Li dendrite growth during the repeated stripping/plating process. The unevenly distributed Li^{+} flux tends to aggregate near the dendrites and further accelerate the dendrite growth, leading to the disastrous increase in "dead Li" and the fragmentation of the SEI layer to further deteriorate the lifespan of the Li metal anode.

The above results indicate that OV-LZO nanotubes with slight graphene as the separator coating facing to the sulfur cathode can adsorb LiPS and improve the interfacial reaction kinetics between electrode and separator, thus restraining the shuttle effect. Meanwhile, OV-LZO nanotubes as the separator coating facing the Li anode can induce uniform and fast

deposition of Li^+ , thus effectively inhibiting Li dendrite growth. Therefore, the Janus separator combining the above two coatings was applied in the Li–S cell to achieve effective synergistic inhibition of Li dendrites and shuttle effects. The cross-section SEM image and elemental mapping illustrates that the average thickness of the OV-LZO/G coating layer facing the S cathode is about 3.3 μm , and that of OV-LZO coating layer facing to Li anode is about 2.6 μm (Figure S21). The integrated Li–S cells were assembled with S/Ketjen black cathodes (sulfur content of 68.7 wt%, Figure S22), an OV-LZO@PP (or LZO@PP, PP) Janus separator and a Cu/Li anode. The N/P ratio (the ratio of the negative electrode capacity to the positive electrode capacity) was controlled at 10 to make the electrochemical performance comparison under a low S loading of 1.5–2.0 mg cm^{-2} . The rate performance was first investigated (Figure S23). Notably, the cell with OV-LZO@PP exhibits superb discharge capacities of 1439.5, 1278.9, 1152.7,

1023.9, 921.2 and 776.1 mAh g^{-1} at 0.2, 0.5, 1, 2, 3 and 5 C, respectively. When the current returns to 0.5 C, a high reversible discharge capacity of 1190.7 mAh g^{-1} remained, suggesting the high sulfur utilization and favorable electrochemical stability enabled by the adsorption/catalysis effect of OV-LZO. The smallest polarization shown by electrochemical curves further reflects the Li_2S deposition/dissolution kinetics corresponding to the rate-determining steps during the discharge/charge process, which were enhanced by OV-LZO (Figure S24). Cycling performance was explored to evaluate the long-term stability. As shown in Figure 4(a), the cell with OV-LZO@PP displays a high reversible capacity of 1098.5 mAh g^{-1} with a low capacity fading rate of 0.055% per cycle and a high CE over 98.5% after 500 cycles. In contrast, the LZO@PP based cell shows a higher capacity fading rate of 0.080% per cycle with CE over 97%, and the cell with the PP separator shows the lowest initial capacity of 589.8 mAh g^{-1} and sharply decreased

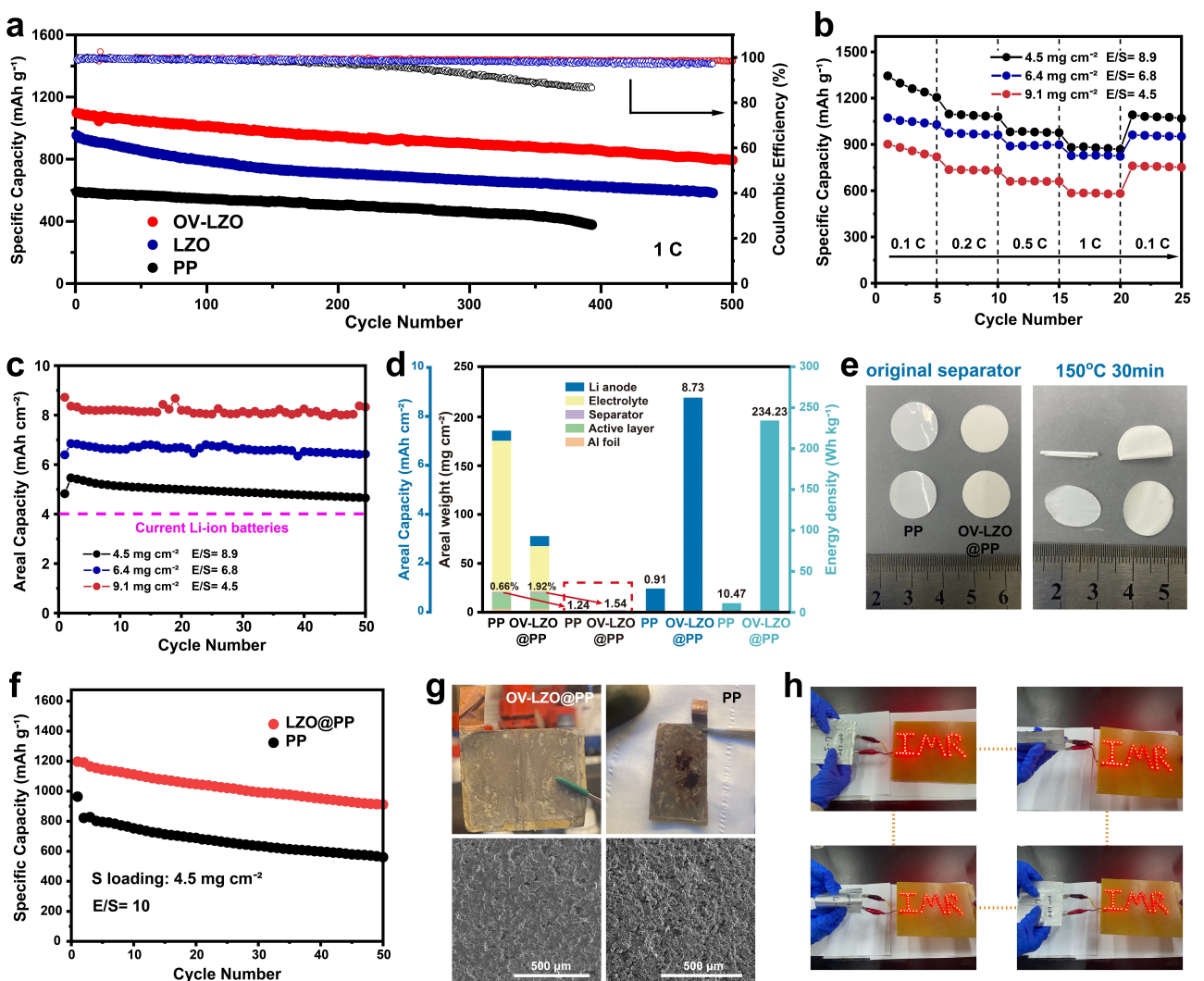


Figure 4. a) Cycling performance of cells with OV-LZO@PP, LZO@PP and PP at 1 C. b) Rate performance at 0.1–1 C and c) cycling performance at 0.2 C of cells with OV-LZO@PP under high sulfur loading, lean electrolyte and low N/P ratio conditions. d) Comparison of the areal weight, areal capacity and energy density of PP and OV-LZO@PP separators. e) Thermal stability tests of PP and OV-LZO@PP. f) Cycling performance of the Li–S pouch cell with PP and OV-LZO@PP at 0.1 C. g) Optical and SEM images of Li foil in the pouch cell based on PP and OV-LZO@PP after cycling. h) LED illumination test by using a Li–S pouch cell based on an OV-LZO@PP separator in various folded states.

CE after 200 cycles. Electrochemical Li plating on Cu foil and the restricted N/P ratio put forward higher requirements for the reversibility of Li stripping/plating at the anode side, which will affect the cycling performance of the Li–S cells more than Li excess conditions. The early CE fading of the cell with the PP separator also reflects the irreversible Li anode reaction.

Li–S cells were further prepared with cathodes that contained a relatively high sulfur loading of 4.5–9.1 mg cm⁻² and reduced the amount of electrolyte (E/S) and N/P (fixed to 2) to achieve competitive areal capacity and energy density with those of state-of-art Li-ion batteries. As depicted in Figure 4(b), the OV-LZO based Li–S cells with (a) S loading of 4.5 mg cm⁻² and E/S of 8.9 mL g⁻¹, (b) S loading of 6.4 mg cm⁻² and E/S of 6.8 mL g⁻¹, and (c) S loading of 9.1 mg cm⁻² and E/S of 5.2 mL g⁻¹ exhibit superior rate capabilities and high discharge capacities of 884.6, 829.2, and 585.1 mAh g⁻¹ even under a current rate of 1 C, respectively. When the current returns to 0.1 C, high reversible discharge capacities of 90.6%, 93.5% and 92.8% can remain, suggesting highly reversible electrochemical processes. The charge/discharge curves of OV-LZO based Li–S cells at different current rate are displayed in Figure S25. All discharge curves exhibit two typical discharge voltage plateaus, manifesting the promoted redox reaction kinetics with the strong catalytic effect of OV-LZO. Moreover, when the S loading was 9.1 mg cm⁻² with an E/S of 4.5 mL g⁻¹, the cell obtained the highest initial areal capacity of 8.7 mAh cm⁻², and 8.33 mAh cm⁻² was maintained after 50 cycles at 0.2 C, which is higher than twice that of state-of-the-art $\text{LiNi}_x\text{Co}_y\text{Mn}_{1-x-y}\text{O}_2$ -based cathodes ($\approx 4 \text{ mAh cm}^{-2}$). The electrochemical performance based on the Janus OV-LZO separator is comparable among state-of-the-art Li–S batteries (Tables S1 and S2).

The effect of separator modification on the gravimetric energy density of Li–S cells can be quantified (Figure 4d). Compared with PP separator (Figure S26), the areal capacity is increased by 9.6 times by Janus OV-LZO@PP separator on the premise of little increase in areal mass loading of separator (from 1.24 to 1.54 mg cm⁻²). In addition, the Janus OV-LZO separator coating achieves much less electrolyte, and the mass proportion of the separator in the Li–S cell increases from 0.66% to 1.92%. Based on the mass of each part of the cell except the packaging material, the gravimetric energy density is increased from 10.47 to 234.23 Wh kg⁻¹ (Table S3), promising Janus OV-LZO modification as an efficient energy boost. What cannot be ignored is that the proportion of electrolyte and positive/negative current collector in all components are still very large. In the actual production, the modification of the cathode, electrolyte and current collector can be integrated to further improve the energy density.

As an important component that separates the cathode and anode, the separator directly determines the safety of the battery. Janus OV-LZO@PP exhibits superior endurance and remains intact even after bending or folding without powder falling off, showing excellent bending resistance (Figure S27). Due to the thermal instability of the polyolefin separator, overheating of the battery environment will bring great potential safety hazards. $\text{La}_2\text{Zr}_2\text{O}_7$, with a fully ordered pyro-

chlore-type structure (Fd-3 m space group) has low thermal conductivity and has been extensively investigated for applications as hosts for thermal barrier coatings in recent years.^[50] The thermal stability of PP and the OV-LZO@PP separator was tested by measuring the dimensional changes of the separators after placing them in an oven preheated to 150°C for 0.5 h (Figure 4e). When a certain pressure is given (press the separator with a stainless-steel sheet), PP shrinks into an ellipse after heating, while OV-LZO@PP is generally round without obvious contraction. When no pressure is given, PP shows an extremely severe curl, while most areas of OV-LZO@PP can still remain smooth. Therefore, the excellent thermal stability of the OV-LZO@PP separator could lower the possibility of shortage under abnormal conditions, which greatly improves the safety performance of the battery.

To achieve wider application visibility, Li–S pouch cells were assembled using a KB/S cathode (S loading of 4.5 mg cm⁻²), Janus OV-LZO@PP (or PP) separator, ~200 μm thick Li anode, and vacuum-sealed aluminum–plastic film, with an E/S ratio of 10 mL g⁻¹ (Figure S28). The Li–S pouch cell with OV-LZO@PP shows a high initial discharge capacity (1169 mAh g⁻¹) and reversible capacity (911 mAh g⁻¹) after 50 cycles, which is significantly higher than that of PP (963.4 mAh g⁻¹ initial and 560.2 mAh g⁻¹ after 50 cycles). The pouch cells in the charging state after cycling were disassembled and the morphology of the Li anode after cycling was investigated (Figure 4g). SEM images show that the Li anode with the PP separator is unevenly corroded by LiPS (Figure S29) and thus may cause uneven Li plating/stripping, Li dendrite growth and repeated breakage of the SEI, resulting in a rough surface morphology. The Li anode with the OV-LZO@PP separator has much smoother morphology by inducing steady Li plating/stripping. The LiPS flux passing through the separator was redistributed by the OV-LZO coating and formed a uniform SEI on the Li surface to further regulate the Li plating/stripping behavior (Figure S30). The electrochemical performance of Li–S pouch cells under sulfur loading of 6.5 mg cm⁻² and lower electrolyte addition (E/S=6) than Li–S coin cell with similar sulfur loading (Figure S31). It can be clearly observed that the Li–S pouch cell with OV-LZO@PP delivers superior initial discharge capacity and reversible capacity (1146.6 mAh g⁻¹) compared to that of PP (565.7 mAh g⁻¹), indicating the greatly suppressed shuttle effect. The discharge/charge profiles of the Li–S pouch cell based on OV-LZO@PP and PP were further investigated. The Li–S pouch cell with OV-LZO@PP exhibits two typical discharge plateaus, while the pouch cell with PP shows invisible voltage plateaus and higher polarization potential due to the limited active sites and sluggish redox kinetics. The flexible battery was directly applied in practical light-emitting diode (LED) illumination tests (Figure 4h). The pouch cell with the OV-LZO@PP separator can steadily power an array of LEDs in various folded states from 0° (flattened) to 180° (folded) and back to 0° (flattened) and even when repeatedly bent, indicating its application potential in flexible Li–S batteries.

Conclusion

In summary, multi-functional OV-LZO nanotubes with surface oxygen vacancies were fabricated as the Janus separator coatings for Li–S batteries to simultaneously tackle the shuttle effect and lithium dendrite issues in Li–S batteries. The overlapping OV-LZO nanotubes construct a highly efficient LiPS adsorption/catalysis network enhanced by oxygen vacancies at the cathode/separator interface. On the anode side, the OV-LZO coating can not only redistribute Li^+ flux, but also construct a fast Li^+ transport network by increasing t_{Li}^+ and boosting Li^+ surface diffusion at the anode/separator interface to achieve highly stable Li plating/stripping. The good thermal stability of OV-LZO lowers the possibility of shortage under abnormal conditions, which ensures the long-term cycling of the battery. As a result, the elaborate Janus separator coating enabled Li–S batteries with initial areal capacities of 8.7 mAh g^{-1} , and 8.33 mAh g^{-1} after 50 cycles at 0.2 C under strict conditions of high sulfur loading (9.1 mg cm^{-2}), lean electrolyte (E/S of 4.5 mL g^{-1}), and low N/P ratio of 2. The gravimetric energy density of the battery was greatly increased compared to that of the PP separator with little increase in the areal mass loading of the separator by OV-LZO. This work provides significant insight into designing a Janus separator to develop high-performance Li–S batteries, which can be integrated with the optimization of other battery components to light the way for the construction of practical Li–S batteries.

Acknowledgements

This work was supported by the National Natural Science Foundation of China (No. 51972313, 52020105010 and 52072378), National Key R&D Program of China (2021YFB3800301 and 2021YFC2800200), the Strategic Priority Research Program of Chinese Academy of Science (No. XDA22010602), Youth Innovation Promotion Association of the Chinese Academy of Sciences (No. Y201942), Liaoning Revitalization Talents Program (No. XLYC1908015 and XLYC2007080) and DNL Cooperation Fund, CAS (DNL202019).

Conflict of Interest

The authors declare no conflict of interest.

Data Availability Statement

The data that support the findings of this study are available from the corresponding author upon reasonable request.

Keywords: Janus separator · lithium dendrite · lithium–sulfur batteries · oxygen vacancy · shuttle effect

- [1] M. Armand, J.-M. Tarascon, *Nature* **2008**, *451*, 652–657.
- [2] P. G. Bruce, S. A. Freunberger, L. J. Hardwick, J.-M. Tarascon, *Nat. Mater.* **2012**, *11*, 19–29.
- [3] A. Manthiram, Y. Fu, S. Chung, C. Zu, Y. Su, *Chem. Rev.* **2014**, *114*, 11751–11787.
- [4] S. Chung, A. Manthiram, *Adv. Mater.* **2018**, *30*, 1705951.
- [5] C. Ma, Y. Feng, X. Liu, Y. Yang, L. Zhou, L. Chen, C. Yan, W. Wei, *Energy Storage Mater.* **2020**, *32*, 46–54.
- [6] Z. Han, S. Li, Y. Wu, C. Yu, S. Cheng, J. Xie, *J. Mater. Chem. A* **2021**, *9*, 24215–24240.
- [7] A. Manthiram, S. Chung, C. Zu, *Adv. Mater.* **2015**, *27*, 1980–2006.
- [8] Q. Pang, X. Liang, C. Y. Kwok, L. F. Nazar, *Nat. Energy* **2016**, *1*, 16132.
- [9] Z. A. Ghazi, X. He, A. M. Khattak, N. A. Khan, B. Liang, A. Iqbal, J. Wang, H. Sin, L. Li, Z. Tang, *Adv. Mater.* **2017**, *29*, 1606817.
- [10] J. Huang, M. Li, Y. Wan, S. Dey, M. Ostwal, D. Zhang, C. W. Yang, C. Su, U. Jeng, J. Ming, A. Amassian, Z. Lai, Y. Han, S. Li, L. Li, *ACS Nano* **2018**, *12*, 836–843.
- [11] Q. Liu, X. Han, Q. Dou, P. Xiong, Y. Kang, S.-W. Kang, B.-K. Kim, H. S. Park, *Batteries & Supercaps* **2021**, *4*, 1843–1849.
- [12] F. Wu, S. Zhao, L. Chen, Y. Lu, Y. Su, Y. Jia, L. Bao, J. Wang, S. Chen, R. Chen, *Energy Storage Mater.* **2018**, *14*, 383–391.
- [13] B. Li, Q. Su, L. Yu, J. Zhang, G. Du, D. Wang, D. Han, M. Zhang, S. Ding, B. Xu, *ACS Nano* **2020**, *14*, 17285–17294.
- [14] Q. Li, Y. Song, R. Xu, L. Zhang, J. Gao, Z. Xia, Z. Tian, N. Wei, M. H. Rummeli, X. Zou, J. Sun, Z. Liu, *ACS Nano* **2018**, *12*, 10240–10250.
- [15] Y. Zhong, X. Xia, S. Deng, J. Zhan, R. Fang, Y. Xia, X. Wang, Q. Zhang, J. Tu, *Adv. Energy Mater.* **2018**, *8*, 1701110.
- [16] Z. Sun, J. Zhang, L. Yin, G. Hu, R. Fang, H.-M. Cheng, F. Li, *Nat. Commun.* **2017**, *8*, 14627.
- [17] R. Wang, C. Luo, T. Wang, G. Zhou, Y. Deng, Y. He, Q. Zhang, F. Kang, W. Lv, Q.-H. Yang, *Adv. Mater.* **2020**, *32*, 2000315.
- [18] Z. Li, J. Zhang, X. W. Lou, *Angew. Chem. Int. Ed.* **2015**, *54*, 12886–12890; *Angew. Chem.* **2015**, *127*, 13078–13082.
- [19] E. Cha, M. D. Patel, J. Park, J. Hwang, V. Prasad, K. Cho, W. Choi, *Nat. Nanotechnol.* **2018**, *13*, 337–344.
- [20] S. Yang, R. Xiao, T. Hu, X. Fan, R. Xu, Z. Sun, B. Zhong, X. Guo, F. Li, *Nano Energy* **2021**, *90*, 106584.
- [21] Z. Ye, Y. Jiang, L. Li, F. Wu, R. Chen, *Adv. Mater.* **2021**, *33*, 2101204.
- [22] P. Li, H. Lv, Z. Li, X. Meng, Z. Lin, R. Wang, X. Li, *Adv. Mater.* **2021**, *33*, 2007803.
- [23] L. Jiao, C. Zhang, C. Geng, S. Wu, H. Li, W. Lv, Y. Tao, Z. Chen, G. Zhou, J. Li, G. Ling, Y. Wan, Q.-H. Yang, *Adv. Energy Mater.* **2019**, *9*, 1900219.
- [24] X. Yang, X. Gao, Q. Sun, S. P. Jand, Y. Yu, Y. Zhao, X. Li, K. Adair, L.-Y. Kuo, J. Rohrer, J. Liang, X. Lin, M. N. Banis, Y. Hu, H. Zhang, X. Li, R. Li, H. Zhang, P. Kaghazchi, T.-K. Sham, X. Sun, *Adv. Mater.* **2019**, *31*, 1901220.
- [25] X. Tao, J. Wang, C. Liu, H. Wang, H. Yao, G. Zheng, Z. W. Seh, Q. Cai, W. Li, G. Zhou, C. Zu, Y. Cui, *Nat. Commun.* **2016**, *7*, 11203.
- [26] G. Li, F. Lu, X. Dou, X. Wang, D. Luo, H. Sun, A. Yu, Z. Chen, *J. Am. Chem. Soc.* **2020**, *142*, 3583–3592.
- [27] F. Pei, L. Lin, A. Fu, S. Mo, D. Ou, X. Fang, N. Zheng, *Joule* **2018**, *2*, 323–336.
- [28] J.-Q. Huang, Q. Zhang, H.-J. Peng, X.-Y. Liu, W.-Z. Qian, F. Wei, *Energy Environ. Sci.* **2014**, *7*, 347.
- [29] X.-B. Cheng, R. Zhang, C.-Z. Zhao, F. Wei, J.-G. Zhang, Q. Zhang, *Adv. Sci.* **2016**, *3*, 1500213.
- [30] Y. Zhao, Y. Ye, F. Wu, Y. Li, L. Li, R. Chen, *Adv. Mater.* **2019**, *31*, 1806532.
- [31] R. Cao, W. Xu, D. Lv, J. Xiao, J.-G. Zhang, *Adv. Energy Mater.* **2015**, *5*, 1402273.
- [32] J. Yan, F. Liu, Z. Hu, J. Gao, W. Zhou, H. Huo, J. Zhou, L. Li, *Nano Lett.* **2020**, *20*, 3798–3807.
- [33] Z. Hao, Y. Wu, Q. Zhao, J. Tang, Q. Zhang, X. Ke, J. Liu, Y. Jin, H. Wang, *Adv. Funct. Mater.* **2021**, *31*, 2102938.
- [34] Y. Liu, S. Xiong, J. Wang, X. Jiao, S. Li, C. Zhang, Z. Song, J. Song, *Energy Storage Mater.* **2019**, *19*, 24–30.
- [35] J. Liang, Q. Chen, X. Liao, P. Yao, B. Zhu, G. Lv, X. Wang, X. Chen, J. Zhu, *Angew. Chem. Int. Ed.* **2020**, *59*, 6561–6566; *Angew. Chem.* **2020**, *132*, 6623–6628.
- [36] W. Li, Y. Zhang, H. Li, Z. Chen, T. Shang, Z. Wu, C. Zhang, J. Li, W. Lv, Y. Tao, Q.-H. Yang, *Batteries & Supercaps* **2020**, *3*, 892–899.
- [37] C. Yan, X.-B. Cheng, Y. Tian, X. Chen, X.-Q. Zhang, W.-J. Li, J.-Q. Huang, Q. Zhang, *Adv. Mater.* **2018**, *30*, 1707629.
- [38] C. Cui, C. Yang, N. Eidson, J. Chen, F. Han, L. Chen, C. Luo, P.-F. Wang, X. Fan, C. Wang, *Adv. Mater.* **2020**, *32*, 1906427.
- [39] W.-G. Lim, S. Kim, C. Jo, J. Lee, *Angew. Chem. Int. Ed.* **2019**, *58*, 18746–18757; *Angew. Chem.* **2019**, *131*, 18920–18931.

- [40] C. Shi, J. Zhu, X. Shen, F. Chen, F. Ning, H. Zhang, Y.-Z. Long, X. Ning, J. Zhao, *RSC Adv.* **2018**, *8*, 4072–4077.
- [41] F. Lei, Y. Sun, K. Liu, S. Gao, L. Liang, B. Pan, Y. Xie, *J. Am. Chem. Soc.* **2014**, *136*, 6826–6829.
- [42] S. A. Ansari, M. M. Khan, S. Kalathil, A. Nisar, J. Lee, M. H. Cho, *Nanoscale* **2013**, *5*, 9238–9246.
- [43] S. N. Ogguguaa, H. C. Swart, O. M. Ntwaeborwa, *Sens. Actuators B* **2017**, *250*, 285–299.
- [44] S. Cheng, J. Wang, S. Duan, J. Zhang, Q. Wang, Y. Zhang, L. Li, H. Liu, Q. Xiao, H. Lin, *Chem. Eng. J.* **2021**, *417*, 128172.
- [45] S. Wang, W. Li, S. Wang, Z. Chen, *J. Eur. Ceram. Soc.* **2015**, *35*, 105–112.
- [46] T. Zeng, Y. Yan, M. He, R. Zheng, D. Du, L. Ren, B. Zhou, C. Shu, *Chem. Commun.* **2021**, *57*, 12687–12690.
- [47] Z. Hao, Q. Zhao, J. Tang, Q. Zhang, J. Liu, Y. Jin, H. Wang, *Mater. Horiz.* **2021**, *8*, 12–32.
- [48] P. Bai, J. Li, F. R. Brushett, M. Z. Bazant, *Energy Environ. Sci.* **2016**, *9*, 3221–3229.
- [49] X.-B. Cheng, R. Zhang, C.-Z. Zhao, Q. Zhang, *Chem. Rev.* **2017**, *15*, 10403–10473.
- [50] K. Bobzin, N. Bagcivan, T. Brogelmann, B. Yildirim, *Surf. Coat. Technol.* **2013**, *237*, 56–64.

Manuscript received: December 13, 2021

Revised manuscript received: January 5, 2022

Accepted manuscript online: January 14, 2022

Version of record online: January 28, 2022